

Breakup of ${}^9\text{Be}$ on ${}^{209}\text{Bi}$ above and near the Coulomb barrier as a molecular single-particle effect: its influence on complete fusion and scattering

A. Diaz-Torres^{a,*}, I.J. Thompson^a and W. Scheid^b

^a*Physics Department, University of Surrey, Guildford GU2 7XH, United Kingdom*

^b*Institut für Theoretische Physik der Justus-Liebig-Universität, D-35392 Giessen, Germany*

(October 27, 2018)

The breakup of the ${}^9\text{Be}$ projectile on the ${}^{209}\text{Bi}$ target at bombarding energies above and near the Coulomb barrier is studied in the adiabatic two-center shell model approach. The effect of ${}^9\text{Be} \rightarrow n + 2\alpha$ breakup channel on complete fusion, elastic and inelastic cross sections is investigated. Results show that the breakup of the projectile ${}^9\text{Be}$ could be due to a molecular single-particle effect shortly before the colliding nuclei reach the Coulomb barrier.

I. INTRODUCTION

A. Review of the subject

The interaction of weakly bound or halo nuclei with stable targets at colliding energies around the Coulomb barrier is a very lively topic due to the increasing interest in nuclear reactions with radioactive beams. The existence and the role of the breakup process of weakly bound projectiles in complete fusion and scattering (elastic and inelastic) mechanisms have been extensively investigated in recent years both theoretically [1–6] and experimentally [7–17], but there is not yet any definitive conclusion.

There are contradictory theoretical works which predict either the suppression [1–4] or the enhancement [5] of the complete fusion cross section due to the coupling of the relative motion of the colliding nuclei to the breakup channel. In a recent paper [6], coupled channels calculations for ${}^{11}\text{Be} + {}^{208}\text{Pb}$ have shown that the coupling of the relative motion to the breakup channel has two effects depending on the value of the bombarding energy, namely the reduction of the complete fusion cross sections at energies above the Coulomb barrier due to the loss of incident flux and the enhancement of the complete fusion cross sections at energies below the Coulomb barrier due to the dynamical renormalisation of the nucleus-nucleus potential. In [1–3], the effects of the breakup process on fusion were studied in the framework of both time-independent and time-dependent semi-classical coupled channels

*Corresponding author.

E-mail address: A.Diaz-Torres@surrey.ac.uk

Fax number: +44 (0)1483 686781

theories using the imaginary part of a local dynamical polarisation potential associated with the breakup channel. In [4], the influence of the breakup process on fusion was studied by solving a three-body Schrödinger equation with a time-dependent wave packet method. The breakup process and its effects on fusion were described in [5,6] in terms of inelastic excitations of the projectile to the continuum within the coupled channels formalism.

In experiments of ${}^9,{}^{10},{}^{11}\text{Be}+{}^{209}\text{Bi}$ [7,10] and ${}^9\text{Be}+{}^{208}\text{Pb}$ [12], it was observed that the breakup process of both ${}^9\text{Be}$ and ${}^{11}\text{Be}$ projectiles suppresses the complete fusion above the Coulomb barrier. Reactions of ${}^6,{}^7\text{Li} + {}^9\text{Be}$ also reveal the same hindrance for fusion [8], although contrary results also exist, e.g., ${}^9\text{Be}+{}^9\text{Be}$ [17]. This fusion hindrance was not observed in the reaction ${}^9\text{Be}+{}^{64}\text{Zn}$ [16]. We expect that the presence or absence of a suppression mechanism in fusion reactions involving ${}^9\text{Be}$ could be associated with the evolution of the last neutron of ${}^9\text{Be}$ in the approach phase of the collision before the nuclei reach the Coulomb barrier, which depends on the structure of the target or projectile. We also expect that molecular effects, which will be discussed later, do not occur in some reactions with ${}^9\text{Be}$. From an optical model analysis of the ${}^9\text{Be}+{}^{209}\text{Bi}$ elastic scattering [15], the imaginary (absorptive) potential at the distance corresponding to the strong interaction radius increases with decreasing bombarding energy towards the Coulomb barrier energy, but this is not the case for the system ${}^9\text{Be}+{}^{64}\text{Zn}$ [16]. This behaviour of the imaginary potential indicates that strong absorption channels are still open for bombarding energies very close to the Coulomb barrier and it was associated with the Coulomb breakup of ${}^9\text{Be}$. Moreover, it was pointed out that other absorption channels related to orientation and deformation effects of ${}^9\text{Be}$ cannot be excluded. Such effects have been reported for the scattering of ${}^9\text{Be}$ by ${}^{40},{}^{44}\text{Ca}$ and ${}^{39}\text{K}$ [18].

B. Object of the work

The aim of this paper is to study the breakup of the ${}^9\text{Be}$ projectile on the ${}^{209}\text{Bi}$ target at energies above and near the Coulomb barrier in the adiabatic two-center shell model (TCSM) [19] approach, as well as its role in the complete fusion and scattering processes. The TCSM is based on the assumption that the nucleons can be described with molecular states during the heavy ion reaction. This means that the motion of the nuclear centers has to be adiabatically slow compared with the rearrangement of the mean field of nucleons. Whether molecular orbitals are formed depends on the ratio of two characteristic times, the collision time $\tau_c \sim 2R/v = 2R(2E/MA)^{-1/2}$ and the nuclear period or single-particle relaxation time $\tau_s \sim 2R/v_{Fermi} = 2R(2\epsilon_F/M)^{-1/2}$, where E is the laboratory bombarding energy, A the projectile mass number, and ϵ_F the Fermi energy in the target or projectile nucleus with valence nucleons. According to the ratio of $\tau_c/\tau_s \sim 3-4$ for the studied reaction, we expect that molecular orbitals and the polarisation of valence nucleons by the field of the other nucleus may have time to develop.

We study the neutron level diagram in the approach phase of this collision in order to see possible single-particle effects (nucleon transfer or single-particle excitations). Since the ${}^9\text{Be}$ has a small separation energy ($S_n = 1.67$ MeV), the breakup channel (${}^9\text{Be} \rightarrow n + {}^8\text{Be}$) could be related to a diabatic single-particle motion of the last neutron of ${}^9\text{Be}$ into the continuum [20] or to a neutron transfer to ${}^{209}\text{Bi}$. Since the nucleus ${}^8\text{Be}$ has no bound states, as the Coulomb field of the target (${}^{209}\text{Bi}$ or ${}^{210}\text{Bi}$) in its vicinity is very strong and the relative

motion is considered adiabatic, we assume that the decay ${}^8\text{Be} \rightarrow 2\alpha$ occurs automatically and immediately. This assumption is experimentally supported by the observation of α particles originating from the decay of ${}^8\text{Be}$ [21]. The capture of a part of the projectile after the breakup is associated with the incomplete fusion channel which will not be considered in the present work for the sake of simplicity.

In general, the neutron promotion from ${}^9\text{Be}$ to ${}^{209}\text{Bi}$ or into the continuum could be related to three types of transitions [22] between the molecular adiabatic single-particle levels: the transition induced by the radial relative motion of nuclei (radial transition $\sim d/dr$), the transition induced by the rotation of the internuclear axis around a fixed axis in the laboratory system (rotational transition $\sim jI$, j and I being the single-particle total angular momentum and the total angular momentum of the system, respectively), or the transition induced by the change of the orientation of the intrinsic symmetry axes of deformed nuclei, which is dependent on the angular momenta of the nuclei ($\sim I'_1, I'_2$ with $I'_1 + I'_2 = I - L$ and L being the orbital angular momentum of the collision). In the TCSM [19] used in the present work, only radial and rotational transitions between the molecular adiabatic single-particle levels can occur because the intrinsic symmetry axis of nuclear shapes lies parallel to the internuclear axis. For arbitrary orientations of the intrinsic symmetry axes of deformed nuclei, a more general TCSM [23] would have to be used. The radial transition occurs between adiabatic states with the same angular momentum projection j_z and is largest at the point of an avoided crossing (pseudo-crossing), while the rotational transition occurs between adiabatic states ϕ_a, ϕ_b with $j_z^a = j_z^b \pm 1$ and is largest at the crossing point of levels. Moreover, the radial excitation mechanism describes the non-adiabaticity of the relative motion (Landau-Zener mechanism [24]) and grows with increasing radial velocity, the diabatic single-particle motion being a limit for large radial transition probabilities [20]. In the diabatic limit of the single-particle motion [20], the nucleons do not occupy the lowest free single-particle levels as in the adiabatic case, but remain in the diabatic levels keeping their quantum numbers during a collective motion of the nuclear system.

The study of single-particle level diagrams [22] can be useful to understand some reaction channels and to simplify coupled channels calculations. A microscopic formulation of the excitation and nucleon transfer in the TCSM and its role in the scattering process of nuclei with loosely bound nucleons was presented in [25] on the basis of the molecular particle-core model. A similar formulation was suggested in [26] in the framework of the orthogonalised coupled-reaction-channel theory. Molecular single-particle effects are experimentally well established phenomena [22] in heavy ion collisions and have been reflected, e.g., in large structures observed in elastic and inelastic excitation functions of reactions between light nuclei.

In sect. 2, trajectories, complete fusion, elastic and inelastic cross sections are calculated in the framework of a classical model, using the potential energy obtained with the adiabatic TCSM along with phenomenological friction coefficients. The role of the breakup of ${}^9\text{Be}$ on complete fusion, elastic and inelastic cross sections is incorporated by using the Landau-Zener approach for the breakup induced by the radial mechanism. We compare the calculated results with experimental data in sect. 3. A summary and conclusions are given in sect. 4.

II. MODEL

A. Adiabatic TCSM

The basic microscopical model for a dinuclear system is the TCSM. The TCSM describes nuclei, namely the united nucleus and the two incoming nuclei. In the TCSM [19] used in the present work, the nuclear shapes are defined by a set of coordinates:

1. The relative distance r between the centers of mass of the two nuclei (or the elongation λ of the system, or the distance $(z_1 - z_2)$ between the centers of the two oscillators).
2. The neck parameter $\varepsilon = E_0/E'$ is defined by the ratio of the actual barrier height E_0 to the barrier height E' of the two-center oscillator. The neck grows with decreasing ε .
3. The transition of the nucleons through the neck is described by the mass (charge) asymmetry $\eta = (A_2 - A_1)/A$ ($\eta_Z = (Z_2 - Z_1)/Z$), where $A_1(Z_1)$ and $A_2(Z_2)$ are the mass (charge) numbers on both sides of the neck and $A = A_1 + A_2$ ($Z = Z_1 + Z_2$).
4. The deformations $\beta_i = a_i/b_i$ ($i = 1, 2$) of axial symmetric fragments are related to the ratio of their semiaxes. For separated nuclei, the semiaxes a_i and b_i can be related to the parameter of quadrupole deformation by using the known expansion of the nuclear surface in spherical harmonics.

In the adiabatic approach, the parameters of the momentum-independent part of the single-particle TCSM potential are determined by the assumption of conservation of the volume enclosed by the nuclear surface, continuity of the potential and its derivatives between the two centres and by the requirement that the TCSM potential barrier with height E_0 is located at $z = 0$. The parameters related to the momentum-dependent part of the potential (spin-orbit and l^2 -like terms) are determined by some interpolation between the appropriate values for the compound nucleus and for the separated fragments for large r . In the present work, the same interpolation method as in [19] is adopted, but the parameters κ and μ of the Nilsson model for the spin-orbit interaction are used [27]. The nuclear-radius constant is $r_0 = 1.2249$ fm and the oscillator quanta are $\hbar\omega_{i0} = 41 \cdot A_i^{-1/3}$ MeV.

The single-particle levels, characterised by the projection j_z of the total angular momentum, are given in the harmonic oscillator potentials only up to constants V_i associated with the depths of the two potential wells. In order to compensate this disadvantage, we use three parameters related to the depths of potential wells of the compound nucleus V_0 and the separated nuclei V_i^∞ for large r . These parameters are expressed by the sum of experimental nucleon separation energies [28–30] and corresponding Fermi levels. For finite relative distances, we interpolate the values of the depth of potential wells V_i as

$$V_i = \left\{ \begin{array}{ll} V_0 + (V_i^\infty - V_0) \frac{\omega_z^i - \omega_z^0}{\varpi_z^i - \omega_z^0}, & \text{if } R_{neck} > 0 \\ V_i^\infty, & \text{if } R_{neck} = 0 \end{array} \right\}, \quad (1)$$

where ϖ_z^i are the frequencies of the oscillator along the internuclear z axis for the configuration of the system with a radius of the neck $R_{neck} = 0$. The ω_z^i and ω_z^0 are the z -oscillator frequencies for the nuclei in the united system and for the compound nucleus, respectively.

It is necessary to point out that V_i are added to the single-particle energies taking care to identify every level in association with its localisation in only one of the two potential wells for separated nuclei.

In order to avoid unrealistic shapes for small relative distances r (compact shapes) and a large mass asymmetry η of the colliding nuclei in this version of the TCSM, it is assumed that the mass asymmetry η decreases, e.g. linearly [19], with decreasing relative distance r from the touching configuration of the nuclei. An adequate shape parametrisation for such highly asymmetric compact configurations was used to study cluster emission in the superasymmetric TCSM [31]. Since the motion of the system is mainly considered in the entrance channel up to relative distances near the touching configuration, the parametrisation used for compact shapes does not influence the results. Moreover, compact shapes of the system do not occur in the approach phase of a collision for bombarding energies above the Coulomb barrier owing to the repulsive core of the nucleus-nucleus potential caused by the centrifugal effect and by diabatic [32,33] or structural forbiddenness effects [34].

The orbital angular momentum independent part of the total potential of the two-center system is calculated with the macroscopic-microscopic method of Strutinsky as

$$V = E_{macr}(r, \varepsilon, \eta, \eta_Z, \beta_1, \beta_2) + \delta E_{shell}(r, \varepsilon, \eta, \eta_Z, \beta_1, \beta_2) + \delta E_{pair}(r, \varepsilon, \eta, \eta_Z, \beta_1, \beta_2) - V_{CN}. \quad (2)$$

The smooth macroscopic part of the potential energy E_{macr} is expressed by the sum of the Coulomb energy E_C and the nuclear surface energy E_N as in the liquid drop model, and they contain a part related to the binding energy of the system and another one related to the nucleus-nucleus interaction potential. In order to take into consideration the finite range of the nuclear force and the diffuse nuclear surface, we use the nuclear surface energy E_N obtained by the Yukawa-plus-exponential method [35] with shapes generated by the TCSM potential. The fluctuating microscopic shell and pairing corrections, δE_{shell} and δE_{pair} , are obtained using the single-particle levels of the TCSM and the Strutinsky method. The dependence of these microscopic corrections on temperature is neglected because the dissipated energy for the studied reaction is only a few MeV [15]. The value of the potential (2) is normalised to the potential energy V_{CN} of the spherical compound nucleus.

B. Classical trajectories

Classical trajectories for a system with reduced mass μ , total energy E and orbital angular momentum $L = \mu r^2 d\varphi/dt$ in the center of mass system, are obtained by solving the generalised Lagrange equations in the relative distance r and orientation φ ($q_i = \{r, \varphi\}$) of the two centers of the nuclei

$$\frac{d}{dt} \left[\frac{\partial \mathcal{L}}{\partial (dq_i/dt)} \right] - \frac{\partial \mathcal{L}}{\partial q_i} = F_i(q, dq/dt) \equiv - \sum_j \gamma_{ij} f_j(q) dq_j/dt, \quad (3)$$

where $\mathcal{L} = T - V$ is the Lagrangian and F_i are the friction forces. As in the surface friction model [36], we assume a diagonal friction tensor $\gamma_{ij} = c_i^0 \delta_{ij}$ (radial and tangential friction) with friction form factors $f_j(q)$. The form factor of the friction forces is calculated as

$$f_{r,\varphi} = [\nabla(E_N - \tilde{E}_N)]^2, \quad (4)$$

\tilde{E}_N being the nuclear surface energy for the configuration of the system with a radius of the neck $R_{neck} = 0$. We have assumed in (4) that frictional effects start with the overlapping of the two nuclei. Theoretical justifications for the classical form of the friction forces were given in [36], where the perturbation theory was used to study the coupling between the collective and the intrinsic degrees of freedom for small overlap between the nuclei. The tangential part of the friction is considerably weaker than the radial part [36]. The phenomenological friction forces in the classical trajectory express the irreversible coupling between the relative motion of nuclei and the degrees of freedom that are not explicitly considered (e.g., collective vibrations of ^{209}Bi), for small overlap between the nuclei outside the touching distance. Moreover, this phenomenological friction does not take into account the reversible coupling (adiabatic single-particle motion due to the Landau-Zener mechanism) between the relative motion and the intrinsic degrees of freedom [37], which is much stronger for large overlap between the nuclei inside the touching distance. The friction parameters c_r^0 and c_φ^0 are usually considered as free parameters and their values are determined from extensive analyses of fusion cross sections and inelastic scattering data for many systems and bombarding energies throughout the periodic table [36,38]. For simplicity, we assume that the reduced mass μ and the friction coefficients c_i^0 do not depend on the temperature of the system. Moreover, the slight increase of the reduced mass with decreasing relative distances for weakly necking shapes around the touching configuration is neglected [39]. In [40], it was pointed out that the inclusion of this contribution does not lead to any appreciable change of the observables in the exit channel. For large overlap between the nuclei, these transport coefficients can be calculated in an adiabatic approach within the linear response theory [41]. In the present work, classical trajectories are calculated using the radial and the tangential friction coefficients $c_r^0 = 4 \times 10^{-23} \text{ MeV}^{-1}\text{s}$ and $c_\varphi^0 = 0.01 \times 10^{-23} \text{ MeV}^{-1}\text{s}$, respectively [36].

C. Complete fusion, elastic and inelastic cross sections

The solution of the classical equations of motion (3) leads to captured and scattered (elastic and inelastic) trajectories. Since the initial mass asymmetry η of the system ($^9\text{Be}+^{209}\text{Bi}$) is larger than its Businaro-Gallone mass asymmetry [33], we assume that the complete fusion channel is mainly related to the relative distance r between the centers of the nuclei. In general, the complete fusion cross section can be expressed as

$$\sigma_{fus} = \sum_{l=0}^{l_{cr}} \sigma_{cap}(\text{E}, l) \cdot P_{CN}(\text{E}, l), \quad (5)$$

where σ_{cap} , P_{CN} and l_{cr} are the partial capture cross section, a hindrance factor for complete fusion and the highest orbital angular momentum (a sharp angular momentum cut-off model) for trajectories which reach the critical distance r_{cr} , respectively. At the critical distance r_{cr} , the shells of the individual nuclei dissolve into those of the compound nucleus [37]. Expression (5) is valid if the mechanism hindering the complete fusion occurs before or after the Coulomb barrier has been passed. The partial capture cross section σ_{cap} is defined as

$$\sigma_{cap} = \frac{\pi \hbar^2}{2\mu\text{E}} (2l + 1) \cdot T_l(\text{E}), \quad (6)$$

where E is the bombarding energy. The transmission coefficient T_l through the Coulomb barrier V_{Bl} with orbital angular momentum $L = l\hbar$ is approximated by that of a parabolic barrier with angular momentum dependent frequency $\hbar\omega_l$

$$T_l(E) = \frac{1}{1 + \exp[2\pi(V_{Bl} - E)/\hbar\omega_l]}. \quad (7)$$

In (5), the factor P_{CN} takes into account other hindrances for the compound nucleus formation. In the reaction ${}^9\text{Be}+{}^{209}\text{Bi}$, we assume that the hindrance is mainly related to the breakup of the projectile ${}^9\text{Be}$ (e.g., ${}^9\text{Be} \rightarrow n+2\alpha$):

$$P_{CN} = 1 - P_{bup}(E, l), \quad (8)$$

where P_{bup} is the breakup probability. The hindrance factor (8) was used in [1–3] and suggested experimentally in [10,12]. The role of P_{bup} in the complete fusion cross section depends on the existence of the breakup channel which is derived, in the present model, from the diagram of neutron levels calculated with the TCSM. Since for orbital angular momenta $0 \leq l \leq l_{cr}$ the breakup probability P_{bup} changes much less than the partial capture cross section σ_{cap} , we use an average value $\overline{P_{bup}}$ with respect to orbital angular momenta. The complete fusion cross section (5) is factorised as

$$\sigma_{fus} = \left[\frac{\pi\hbar^2}{2\mu E} \sum_{l=0}^{l_{cr}} \frac{2l+1}{1 + \exp[2\pi(V_{Bl} - E)/\hbar\omega_l]} \right] \cdot (1 - \overline{P_{bup}}(E)). \quad (9)$$

For simplicity, we introduce the approximations [43] $\hbar\omega_l = \hbar\omega$ and $r_{Bl} = r_B$, with $\hbar\omega$ and r_B being the frequency and the position of the $l = 0$ Coulomb barrier V_B , respectively. Moreover, the summation in Eq. (9) is replaced by an integration and the term in brackets yields an analytical expression as the formula for the complete fusion cross section in the Glas-Mosel model [43]. The Glas-Mosel model is used, instead of a dynamical fusion model as the dynamical energy surplus model [44], to calculate complete fusion cross sections without breakup because we found that the radial kinetic energy loss of nuclei (${}^9\text{Be}+{}^{209}\text{Bi}$) before reaching the Coulomb barrier is negligible compared with the static Coulomb barrier V_B , e.g., ≤ 0.1 MeV at the bombarding energy $1.15V_B$ ($E_{c.m.} = 46$ MeV) for $0 \leq l \leq l_{cr}$. However, frictional effects on the radial motion of nuclei are important in calculating the breakup probability P_{bup} because this probability exponentially depends on the radial velocity of nuclei as we will discuss further on.

In the complete fusion process, the probability for a breakup process induced by the Landau-Zener mechanism at an isolated pseudo-crossing of adiabatic single-particle levels can be expressed as

$$P_{bup} = P_{LZ}^{(e)}, \quad (10)$$

and in the scattering process as

$$P_{bup} = P_{LZ}^{(e)} + (1 - P_{LZ}^{(e)}) \cdot P_{LZ}^{(lv)}, \quad (11)$$

since the system passes through the pseudo-crossing point twice, first entering (e) and then leaving (lv) the interaction region. Here, we have made a distinction between (e) and (lv)

because the radial velocity changes due to frictional effects. The first term in Eq.(11) is $P_{LZ}^{(e)}$, instead of $P_{LZ}^{(e)} \cdot (1 - P_{LZ}^{(lv)})$, because of our assumption of an immediate breakup of ${}^8\text{Be} \rightarrow 2\alpha$ after the neutron in ${}^9\text{Be}$ has been removed from the nucleus entering the interaction region (the neutron does not get bound again with ${}^8\text{Be}$ when the nuclei leave the interaction region). At an isolated pseudo-crossing of adiabatic single-particle levels E_1, E_2 for a relative distance r_0 , the Landau-Zener probability [24] for a nucleon transition between the single-particle levels is

$$P_{LZ} = e^{-2\pi G^0}, \quad (12)$$

with

$$G^0 = \frac{|H'_{12}|^2}{\hbar v^0 \left| \frac{d}{dr}(\epsilon_1 - \epsilon_2) \right|_{r=r_0}}, \quad (13)$$

where $|H'_{12}|$ is a coupling matrix element between the diabatic states ϵ_1, ϵ_2 and is equal to half the closest distance between the adiabatic levels E_1, E_2 at r_0 . Diabatic states ϵ_1, ϵ_2 are a set of states which run smoothly through the crossing. The radial velocity v^0 , which is the only quantity concerning relative motion in the above expression, can be calculated from the classical equations of motion (3). Since the radial velocity v^0 depends on the incident energy E and the orbital angular momentum l , P_{LZ} depends also on E and l . The Landau-Zener formula is derived under the following assumptions: H'_{12} is smaller than the relative kinetic energy of the nuclei, $(\epsilon_1 - \epsilon_2)$ is a linear function of r , and v^0 is constant. The restriction to constant velocities implies that the point of avoided level crossing is far from the turning point of the relative motion of the two nuclei. The assumption of a constant relative velocity can be approximately fulfilled in a region where the nucleus-nucleus potential is shallow. In general, the neutron transition at a pseudo-crossing can be calculated semiclassically [22] using a time-dependent Schrödinger equation for the neutron wave function expanded in a basis of two diabatic wave functions related to the diabatic levels ϵ_1, ϵ_2 and a classical equation for the radial relative motion of the nuclei.

The scattering function $\theta(l)$ is calculated from the classical trajectories. Elastic and inelastic scattering cross sections σ are obtained from the classical scattering cross section σ_{cl} as

$$\frac{d\sigma}{d\Omega} = \frac{b(\theta)}{\sin\theta} \left| \frac{db(\theta)}{d\theta} \right| \cdot P_{sc}, \quad (14)$$

where the classical scattering cross section σ_{cl} is given in terms of the scattering angle θ and of the impact parameter $b = l\hbar/\sqrt{2\mu E}$. The hindrance factor for scattering $P_{sc} = 1 - P_{bup}$ (P_{bup} is obtained from Eq. (11)) takes into account the fact that the number of scattered projectiles is reduced by the breakup process. We define as elastic events those non-captured trajectories which show less than 0.5 MeV energy loss, and as inelastic ones all other non-captured trajectories.

III. RESULTS OF THE CALCULATION AND DISCUSSION

Since the collision above the Coulomb barrier is discussed, we first consider ${}^9\text{Be}$ and ${}^{209}\text{Bi}$ as spherical nuclei (ratio of the semiaxes $\beta_i = 1$), and then study the deformation effects.

The assumption of spherical nuclei is suitable if the change of the nucleus-nucleus potential, due to orientation and deformation effects of the nuclei, is small in comparison with the surplus of bombarding energy above the potential. It is known [38] that the deformation effects in the entrance channel may be important for collisions very close to the Coulomb barrier, where they mostly cause an increase of the complete fusion cross section.

In order to obtain a nuclear shape for the touching configuration of the nuclei similar to the one supplied by the overlap of the two nuclear frozen densities [32,33,42], the neck parameter ε should be set at about 0.75. With this value of ε , the neck radius and the distance between the centers of the nuclei are approximately equal to the corresponding quantities in the dinuclear system formed by the overlap of the two frozen densities.

A. Neutron level diagram of the adiabatic TCSM

Fig. 1 shows the neutron level diagram of the TCSM for the system ${}^9\text{Be} + {}^{209}\text{Bi} \rightarrow {}^{218}\text{Fr}$ as a function of the relative distance r between the spherical nuclei. For $r \approx 5.5$ fm (the relative distance between the centers of mass of the two hemispheres of the spherical compound nucleus), we recognise the neutron single-particle states of the spherical compound nucleus ${}^{218}\text{Fr}$ and for large r the neutron single-particle states of the spherical separated nuclei ${}^9\text{Be}$ and ${}^{209}\text{Bi}$. The quantum numbers l, j for these asymptotic neutron levels are shown. The single-particle levels quickly change in the vicinity of $r \approx 5.5$ fm because of the abrupt change of the nuclear shape from a spherical shape (at $r \approx 5.5$ fm) to compact asymmetric shapes with a large value of the neck parameter $\varepsilon = 0.75$ (for $r \gtrsim 5.5$ fm). Small values of the neck parameter ε (0 – 0.2) are more realistic for such compact shapes near the spherical shape because the potential energy of the system decreases with decreasing values of ε [22]. The nuclei ${}^9\text{Be}$ and ${}^{209}\text{Bi}$ only reach spherical shapes for large r due to a polarisation effect caused by the smoothing of the barrier which joins the two oscillator potential wells [19]. This evolution to spherical shapes depends slightly on the value of the neck parameter ε . In Fig. 1, L^* and H^* denote the highest occupied level for the nuclei ${}^9\text{Be}$ and ${}^{209}\text{Bi}$, respectively. The large gap for the neutron subsystem of ${}^{209}\text{Bi}$ associated with the neutron magic number $N=126$ is observed. The internal arrow (A) indicates the distance $r_t = 9.82$ fm corresponding to the touching configuration of the nuclei and the external one (C) indicates the relative distance $r = 13.15$ fm for the configuration of the system with a radius of the neck $R_{neck} = 0$. The Coulomb barrier (B) is located between these two arrows at $r_B = 11.4$ fm.

In Fig. 1 at $r \approx 12$ fm, we can see two very close pseudo-crossings (denoted by 1 and 2) between the highest occupied state of ${}^9\text{Be}$ with $j_z = 3/2$ and two unoccupied states of ${}^{209}\text{Bi}$ with $j_z = 3/2$. Pseudo-crossings (denoted by 3 and 4) between these states also occur at relative distances close to the touching configuration of the nuclei. The level denoted by L corresponds to a level of ${}^9\text{Be}$ with $j_z = 1/2$, occupied by two neutrons. This level shows a pseudo-crossing (denoted by 5) at $r \approx 12.5$ fm with an unoccupied state of ${}^{209}\text{Bi}$ with $j_z = 1/2$ as well as a crossing (denoted by 6) with another state of ${}^{209}\text{Bi}$ with $j_z = 3/2$. In general, at pseudo-crossings 1-5 transitions induced by a radial mechanism can occur. The rotational mechanism can induce a transition at crossing 6, although this type of transition is much weaker than the radial one [22]. The radial transitions 1-4 are associated with the most favourable breakup channel ${}^9\text{Be} \rightarrow n+2\alpha$ ($Q = -1.57$ MeV).

In the present work, we will only consider transitions at the pseudo-crossings 1-2 of Fig. 1. The last neutron of ${}^9\text{Be}$ could be promoted into the continuum at pseudo-crossing 1 and could be transferred to ${}^{209}\text{Bi}$ at pseudo-crossing 2. At the pseudo-crossings 1-2, the applicability of the Landau-Zener approach is quite good. The values of $|H'_{12}|$ and $\frac{d}{dr}(\epsilon_1 - \epsilon_2)$ at the pseudo-crossings 1-2 are 0.1073 MeV, 0.0184 MeVfm $^{-1}$ and 0.1250 MeV, 0.0352 MeVfm $^{-1}$, respectively. It could be expected that transition probabilities at pseudo-crossings 3-4 are much smaller than at pseudo-crossings 1-2, because the radial velocity decreases at the touching configuration of the nuclei due to strong frictional effects.

From the neutron level diagram, one can observe that the shells of individual nuclei dissolve into those of the compound nucleus between 7.5 – 10 fm, which agree with the empirical critical distance $r_{cr} = 8.01$ fm obtained by Galin's formula [46]. We will use the value r_{cr} obtained by Galin's formula as the critical distance. It is important to note that the crossing and the pseudo-crossing of levels occur nearly at the same relative distances, independent of large variations in the parameter sets of the TCSM.

B. Nucleus-nucleus potential

Fig. 2a) shows the total nucleus-nucleus potential for zero orbital angular momentum of colliding nuclei as a function of the relative distance r between the spherical nuclei (solid curve). We compare the results to those obtained using a total nucleus-nucleus potential (dashed curve) which is calculated as the sum of experimental binding energies [47] of the nuclei ($B_1 + B_2 - B_{12}$) and a sudden nucleus-nucleus interaction potential. The B_1 , B_2 and B_{12} are the experimental binding energies of the colliding nuclei and the compound nucleus, respectively. The sudden nucleus-nucleus interaction potential is obtained with the double-folding method using the Skyrme-type effective density-dependent nucleon-nucleon interaction and a realistic two-parameter symmetrised Woods-Saxon function for the density of nuclei [42]. Microscopic corrections to the double-folding potential are included in the binding energies.

For large relative distances and for relative distances around the barrier, the potential calculated with the adiabatic TCSM is similar to the potential obtained with the double-folding method and small differences are explained by different nuclear shapes used in the two approaches. The height and the frequency $\hbar\omega$ of the barrier for both total nucleus-nucleus potentials are about 26 MeV and 2 MeV, respectively. For relative distances smaller than the position r_B of the barrier, the adiabatic TCSM-potential decreases slower than the double-folding potential because of a slower decrease of the macroscopic nuclear surface energy (Fig. 2b). Fig. 2a) also shows the adiabatic TCSM-potential around the barrier for the prolate deformed nuclei in the pole-to-pole configuration (dashed-dotted curve), where the static deformations (ratio of the semiaxes) of ${}^9\text{Be}$ [45] and ${}^{209}\text{Bi}$ are taken as $\beta_1 = 1.2$ and $\beta_2 = 1.05$, respectively. The deformations also take the effects of polarisation of the nuclei into account, induced by the mean-field of the partner-nucleus. In this case, the value of the barrier decreases by ~ 1.3 MeV, with approximately the same frequency $\hbar\omega$, and its position is shifted to $r_B \approx 11.5$ fm. The role of this potential for complete fusion very close to the barrier will be discussed further on.

In Fig.2b), the nuclear surface energy E_N is normalised to the nuclear surface energy \tilde{E}_N for the configuration of the system with a radius of the neck $R_{neck} = 0$. The small increase

of this energy at $r \approx 12.5$ fm is related to the formation of a neck between the colliding nuclei. The double-folding potential shows a repulsive core for small relative distances which reflects the action of the Pauli principle in the Skyrme-type effective density-dependent nucleon-nucleon interaction. The numerical values of this sudden potential are similar to the diabatic potential [32] even though both potentials are conceptually and physically not equivalent. The repulsive character of the diabatic potential is mainly related to diabatic particle-hole excitations. We would like to stress that there is practically no difference between the adiabatic and diabatic potentials of the two nuclei for relative distances larger than the one corresponding to the touching configuration, because the number of pseudo-crossings of single-particle levels is very small [32,33].

C. Complete fusion cross section and breakup process

Fig. 3 shows the complete fusion cross section σ_{fus} as a function of the inverse of the bombarding energy in the center of mass system $1/E_{c.m.}$. Experimental fusion cross sections (full dots) for ${}^9\text{Be} + {}^{209}\text{Bi}$ are from [10]. It was pointed out in [10] that the experimental fusion data for ${}^9\text{Be} + {}^{209}\text{Bi}$ include the complete fusion of ${}^{8,9}\text{Be}$. In [10], it was assumed that the ${}^8\text{Be}$ dissociation after the breakup of ${}^9\text{Be}$ ($\rightarrow n + {}^8\text{Be}$) occurs in a time much longer than the reaction one. However, we assume the opposite that the decay ${}^8\text{Be} \rightarrow 2\alpha$ occurs automatically and immediately once ${}^9\text{Be}$ breaks up before reaching the Coulomb barrier. The capture either of 2α particles by the target ${}^{210}\text{Bi}$ (in the case of the neutron transfer) or of all projectile fragments ($n + 2\alpha$) by the target ${}^{209}\text{Bi}$ (in the case of the neutron single-particle motion into the continuum) can also occur and, therefore, contribute to experimental complete fusion cross sections. We do not include these events because this is in itself a complex problem that needs to be investigated further. The occurrence of these events as well as the incomplete fusion process depend on both kinematical aspects of the reaction (e.g., the angle between the 2α particles, which depends on bombarding energy) and dynamical aspects (e.g., motion of 2α particles in the mean field of the target). Hence, the present calculations yield a lower limit for complete fusion cross sections. Comparing this lower limit with the experimental complete fusion cross sections, we expect that the capture of all individual components of ${}^9\text{Be}$ by the target, after the ${}^9\text{Be}$ breakup, is not very significant. Our results are also compared with the experimental complete fusion cross sections (full triangles) obtained for the similar reaction ${}^9\text{Be} + {}^{208}\text{Pb}$ [12].

In Fig. 3, we can see that the theoretical complete fusion cross sections calculated with expression (9) (dotted curve) agree well with the experimental complete fusion cross sections. The adiabatic TCSM-potential for the spherical nuclei is used for these calculations and the results weakly depend on the value of the critical distance r_{cr} . Predictions (without breakup) of the Glas-Mosel model for this nucleus-nucleus potential are shown by a solid curve. The theoretical hindrance factor $(1 - \overline{P_{bup}}(E_{c.m.}))$ for complete fusion changes with increasing bombarding energy from 0.76 (24% of breakup) for bombarding energies 1.05 times the value of the Coulomb barrier to 0.66 (34% of breakup) for bombarding energies about 1.15 times the value of the Coulomb barrier. These values agree with the experimental value of ~ 0.75 obtained for the studied reaction [10] and with the experimental value of 0.68 ± 0.07 reported in [12] for the similar reaction ${}^9\text{Be} + {}^{208}\text{Pb}$. The calculation of complete fusion cross sections with breakup (dotted curve in Fig. 3) stops at the bombarding energy 1.05 times

the value of the Coulomb barrier for two reasons, namely the assumption of spherical nuclei is not suitable for bombarding energies very close to the Coulomb barrier and the breakup probability (9) cannot be calculated with the Landau-Zener formula (12) for sub-coulomb trajectories because a radial velocity of the nuclei is not defined in the classically forbidden region. The arrow in Fig. 3 indicates the value of the Coulomb barrier of the adiabatic TCSM-potential for the spherical nuclei which is about 40 MeV. The value of the Coulomb barrier is obtained by subtracting $(B_1 + B_2 - B_{12})$ from the value of the barrier of the total nucleus-nucleus potential of Fig. 2a).

In Fig. 3, the dashed-dotted curve shows the complete fusion cross sections calculated with the Glas-Mosel model (without breakup) for the adiabatic TCSM-potential with prolate deformed nuclei in the pole-to-pole configuration. The complete fusion cross section for bombarding energies very close to the Coulomb barrier can increase due to static deformation and orientation effects which lower the value of the Coulomb barrier to ~ 38.7 MeV. Due to the deformation effects and to the orientation of the intrinsic symmetry axes of deformed nuclei, the height of the Coulomb barrier can be larger or smaller than the one obtained with spherical nuclei. The complete fusion cross section for bombarding energies very close to the Coulomb barrier can be considered as an averaged value for different orientations of the intrinsic symmetry axes of the deformed nuclei. It could be expected that the role of the breakup (Fig. 4, discussed further on), suppressing the complete fusion (9), is reduced for decreasing bombarding energies towards energies below the Coulomb barrier, and an enhancement of the complete fusion can be a result of large transmission coefficients for the smaller fusion barriers associated with certain orientations (e.g., pole-to-pole) of the deformed nuclei.

Fig. 4 shows the breakup probability P_{bup} as a function of the orbital angular momentum l of captured trajectories ($0 \leq l \leq l_{cr}$) for two values of the bombarding energy $E_{c.m.}$, namely 42 MeV (dashed curve) and 46 MeV (solid curve). The breakup probability P_{bup} is calculated as the product of two independent Landau-Zener transitions (12) at the very close pseudo-crossings 1-2, respectively, of Fig. 1. For $0 \leq l \leq l_{cr}$ and $E_{c.m.} = 42$ MeV (46 MeV), the breakup probability P_{bup} decreases by a factor 1.3 (1.7) whereas the partial capture cross section σ_{cap} (6) increases by a factor 6.5 (10.5). For a fixed bombarding energy $E_{c.m.}$, the breakup probability decreases with increasing orbital angular momentum l because the potential energy increases and the radial velocity (kinetic energy) decreases at the pseudo-crossing points. For a fixed orbital angular momentum l , the radial velocity at the pseudo-crossing points and, therefore, the breakup probability increases with an increasing bombarding energy. Results are similar to those obtained when the double-folding potential determines the trajectories.

D. Elastic and inelastic scattering cross sections

For a bombarding energy $E_{c.m.} = 46$ MeV, Fig. 5 shows the scattering function $\theta(l)$ (upper part), the radial distance r_{min} of closest approach of the nuclei (middle part), and the dissipated energy E_{diss} (lower part) as a function of the orbital angular momentum l for non-captured trajectories, using two different potentials. For small orbital angular momenta l , the TCSM results (solid curve) are quite similar to those obtained using the double-folding potential (dot-dashed curve). Differences mainly appear for large values of l

due to the different tails of the nucleus-nucleus potential. For the adiabatic TCSM-potential with spherical nuclei, we can observe that inelastic events are associated with low orbital angular momenta ($12 - 22\hbar$) corresponding to angles smaller than the rainbow angle θ_r [22] (where the scattering function $\theta(l)$ has a local maximum). The dissipated energies for these trajectories are a few MeV. The results do not depend strongly on the value of the radial friction coefficient c_r^0 (Fig.6, upper part). Since most of these inelastic trajectories show a turning point inside the radius of the pseudo-crossings 1-2 of Fig. 1, their classical inelastic cross sections are reduced by the effect of the breakup of ${}^9\text{Be}$. For trajectories with $l = 12 - 16\hbar$, the classical turning point is relatively far from the position of the pseudo-crossings 1-2 ($r \approx 12$ fm) and we use the Landau-Zener approach to calculate the breakup probabilities P_{bup} . In Eq. (11), the transition probabilities $P_{LZ}^{(e)}$ and $P_{LZ}^{(lv)}$ are calculated as in the complete fusion channel.

Fig. 6 (middle part) shows the angular distribution of inelastic events. The classical inelastic angular distributions depend weakly on the radial friction coefficient c_r^0 . They slightly change due to small shifts of the rainbow angle θ_r between $90 - 95^\circ$ corresponding to dissipated energies between $1.5 - 3$ MeV for the scattered trajectories with the rainbow angle θ_r . Classical inelastic cross sections are very large in the neighbourhood of the rainbow angle (rainbow scattering) and the cross section becomes infinite at θ_r . Since the projectile ${}^9\text{Be}$ has no excited bound states, the inelastic events are related to the excitation of the target ${}^{209}\text{Bi}$. The breakup of ${}^9\text{Be}$ reduces the classical inelastic cross sections by $29 - 34\%$ for scattering angles smaller than the rainbow angle θ_r , but their values still remain appreciable. The experimental point is extracted from [15] and corresponds to the maximum of the angular distribution of the inelastic collective (vibrational) multiplet 3^- of ${}^{209}\text{Bi}$ at around 2.6 MeV for a scattering angle of 95° . This multiplet could not be observed at angles smaller than $\sim 90^\circ$, which was explained by an increasing background *most probably originating from the tail of the elastic peak*. The large values of the elastic cross section (one-two orders of magnitude larger than the inelastic one) for angles smaller than $\sim 90^\circ$ support this claim (Fig. 6, lower part). This reason could also explain that all the other ${}^{209}\text{Bi}$ inelastic channels were observed with negligible cross sections [15].

We have assumed that a corresponding classical trajectory is associated with the peak of the experimental angular distribution for this inelastic channel. Moreover, the classical trajectory corresponds to the mean trajectory. In fact, the width of the experimental angular distribution for a given inelastic channel is caused by quantal effects and statistical fluctuations [38]. Although the experimental point of Fig. 6 (middle part) cannot be reproduced in the present classical treatment, we would like to note that the classical trajectory corresponding to the dissipated energy of 2.6 MeV has a scattering angle very close to the experimental one being in the vicinity of the rainbow angle θ_r . In reality the classical singularity at the rainbow angle is removed due to quantal effects, statistical fluctuations and also experimental broadening [38]. For example, the inelastic angular distribution in the semiclassical approximation for rainbow scattering [22] using the Airy formula shows a smooth exponential decrease from ~ 200 mb to ~ 100 mb with increasing scattering angles around the rainbow angle θ_r . However, the semiclassical method of scattering [22] is not appropriate for the reaction studied here because the reduced mass μ of the system is very small and the value of de Broglie wavelength $h/\sqrt{2\mu E}$ of nuclei in the relative motion is comparable to their nuclear radii. The experimental value in Fig. 6 (middle part) could be

on the “dark side” ($\theta > \theta_r$) of the angular pattern of rainbow scattering. This experimental value of the inelastic cross section can, however, well be reproduced by the coupled channels method [15], where the relative motion of the nuclei is treated quantum mechanically.

Fig. 6 (lower part) shows the angular distribution of elastic events, normalised to the Rutherford cross section σ_R . For smaller scattering angles, the elastic cross section obtained with the adiabatic-TCSM potential slightly deviates from the Rutherford cross section due to the deviation of the tail of the adiabatic TCSM-potential from the Coulomb tail for large r . The increasing values around $\sim 90^\circ$ occur because the scattering angles are near the rainbow angle θ_r . The effect of the breakup in the elastic scattering is not considered because the turning point for elastic trajectories is outside the radius of the pseudo-crossings 1-2 of Fig. 1. Results obtained when the double-folding potential determines the elastic trajectories are closer to the experimental data.

For decreasing bombarding energies, the reduction of the projectile penetration leads to a decrease of the dissipated energy for inelastic events. We found that the rainbow angle θ_r in the scattering function $\theta(l)$ disappears for $E_{c.m.} \approx 44$ MeV. The scattering angle for inelastic trajectories ($E_{diss} \geq 0.5$ MeV) becomes larger than 95° increasing to larger angles with decreasing bombarding energies. Inelastic cross sections become smaller with decreasing bombarding energies because the increase of $d\theta(l)/dl$ is larger than the increase of the prefactor of (14) proportional to $E_{c.m.}^{-1}$. Moreover, the breakup probability P_{bup} of ${}^9\text{Be}$ decreases with decreasing bombarding energies for inelastic trajectories ($E_{diss} \geq 0.5$ MeV) where the radial distance r_{min} of closest approach is smaller than ~ 12 fm (inelastic events with smaller values of l). This probability changes with decreasing bombarding energy from 0.34–0.29 ($l = 12 - 16\hbar$) for bombarding energies 1.15 times the value of the Coulomb barrier to 0.2 – 0.11 ($l = 8 - 10\hbar$) for bombarding energies about 1.05 times the value of the Coulomb barrier. As in the complete fusion channel, the effect of the breakup of ${}^9\text{Be}$ on inelastic cross sections is diminished with decreasing bombarding energies.

IV. SUMMARY AND CONCLUSIONS

The breakup of the ${}^9\text{Be}$ projectile on the ${}^{209}\text{Bi}$ target at bombarding energies above and near the Coulomb barrier has been studied in the adiabatic two-center shell model approach as well as its effect on the complete fusion and scattering processes. The neutron level diagram of the two-center shell model reveals two very close pseudo-crossings between the state $j_z = 3/2$ of the last neutron of ${}^9\text{Be}$ and two unoccupied states of ${}^{209}\text{Bi}$ with the same projection of the single-particle total angular momentum j_z , shortly before the colliding nuclei reach the Coulomb barrier. A radial velocity-dependent transition of the last neutron of ${}^9\text{Be}$ into the continuum and to ${}^{209}\text{Bi}$ at these pseudo-crossings of molecular levels leads to the most favourable breakup channel of ${}^9\text{Be}$ (${}^9\text{Be} \rightarrow n + {}^8\text{Be}$). Since the nucleus ${}^8\text{Be}$ has no bound states, the Coulomb field of the target (${}^{209}\text{Bi}$ or ${}^{210}\text{Bi}$) in its vicinity is very strong and the relative motion of the nuclei is considered adiabatic, we assumed that the decay ${}^8\text{Be} \rightarrow 2\alpha$ occurs automatically and immediately. Breakup probabilities depending on the bombarding energy and the orbital angular momentum have been calculated with the Landau-Zener approach and trajectories obtained from a classical model using the adiabatic TCSM-potential along with phenomenological friction coefficients.

The effect of this breakup channel on complete fusion and scattering (elastic and inelastic)

cross sections was studied. From the value obtained with the Glas-Mosel model without breakup, the complete fusion cross section reduces by 34% for the bombarding energy 1.15 times the value of the Coulomb barrier and by 24% for the bombarding energy 1.05 times the value of the Coulomb barrier. Calculated complete fusion cross sections agree with the experimental data. The breakup probability of ${}^9\text{Be}$ decreases with decreasing bombarding energies towards the Coulomb barrier, with a hindrance factor of $0.66 - 0.76$ for complete fusion which is similar to the experimental one of ~ 0.75 obtained for the studied reaction and to the experimental value of 0.68 ± 0.07 for the similar reaction ${}^9\text{Be} + {}^{208}\text{Pb}$. For a fixed bombarding energy, the breakup probability increases with decreasing orbital angular momentum and it becomes maximal for a central collision.

The effect of the breakup of ${}^9\text{Be}$ on inelastic channel is similar to its effect on complete fusion channel. Inelastic cross sections decrease with decreasing bombarding energies. Results obtained for $E_{\text{c.m.}} = 46$ MeV qualitatively explain the experiment. The results are similar to those obtained when the double-folding potential determines the trajectories.

In general, the results indicate that absorption channels for bombarding energies very close to the Coulomb barrier observed in experiment [15] can also be associated with orientation and static deformation effects of ${}^9\text{Be}$ which lower the value of the Coulomb barrier and increase the fusion cross section. Our results also support the molecular description of the highly asymmetric reaction ${}^9\text{Be} + {}^{209}\text{Bi}$ in the framework of the two-center shell model. It would be interesting to study other reactions with ${}^9\text{Be}$ but a more general two-center shell model [23] would be needed in order to describe, e.g., arbitrary orientations of the intrinsic symmetry axes of deformed nuclei. Calculations for the studied reaction using a three-body model within a coupled discretised continuum channels (CDCC) formalism are in progress.

Acknowledgments

The authors would like to thank Dr. G.G. Adamian and Dr. N.V. Antonenko for a careful reading of the manuscript, fruitful discussions and suggestions, and Mrs. N. Diaz-Torres for her help in preparing the paper. We would like particularly to thank Prof. C. Signorini and Dr. M. Dasgupta for their experimental data. UK support from the EPSRC grant GR/M/82141 is acknowledged.

-
- [1] M.S. Hussein, M.P. Pato, L.F. Canto and R. Donangelo, Phys. Rev. C 46 (1992) 377; Phys. Rev. C 47 (1993) 2398.
- [2] L.F. Canto, R. Donangelo, P. Lotti and M.S. Hussein, Phys. Rev. C 52 (1995) R2848.
- [3] N. Takigawa, M. Kuratani and H. Sagawa, Phys. Rev. C 47 (1993) R2470.
- [4] K. Yabana, Prog. Theor. Phys. 97 (1997) 437.
- [5] C.H. Dasso and A. Vitturi, Phys. Rev. C 50 (1994) R12.
- [6] K. Hagino, A. Vitturi, C.H. Dasso and S.M. Lenzi, Phys. Rev. C 61 (2000) 037602.
- [7] A. Yoshida et al., Phys. Lett. B 389 (1996) 457.
- [8] J. Takahashi et al., Phys. Rev. Lett. 78 (1997) 30.
- [9] K.E. Rehm et al., Phys. Rev. Lett. 81 (1998) 3341.
- [10] C. Signorini et al., Eur. Phys. J. A 2 (1998) 227; Eur. Phys. J. A 5 (1999) 7.
- [11] J.J. Kolata et al., Phys. Rev. Lett. 81 (1998) 4580.
- [12] M. Dasgupta et al., Phys. Rev. Lett. 82 (1999) 1395.
- [13] M. Trotta et al., Phys. Rev. Lett. 84 (2000) 2342.
- [14] E.F. Aguilera et al., Phys. Rev. Lett. 84 (2000) 5058.
- [15] C. Signorini et al., Phys. Rev. C 61 (2000) 061603.
- [16] S. B. Moraes et al., Phys. Rev. C 61 (2000) 064608.
- [17] A. Mukherjee and B. Dasmahapatra, Nucl. Phys. A 614 (1997) 238; Phys. Rev. C 63 (2000) 017604.
- [18] V. Hnizdo et al., Phys. Rev. Lett. 46 (1981) 590; Phys. Rev. C 24 (1981) 1495.
- [19] J. Maruhn and W. Greiner, Z. Phys. 251 (1972) 431.
- [20] W. Cassing and W. Nörenberg, Nucl. Phys. A 431 (1984) 558; Nucl. Phys. A 438 (1985) 253.
- [21] C. Signorini et al., in *Proc. of Int. Conference BO2000*, Bologna, Italy, May 2000, eds. D. Vretenaar et al., (World Scientific, Singapore) in press.
- [22] W. Greiner, J.Y. Park and W. Scheid, in *Nuclear Molecules*, (World Scientific Publishing Co. Inc, 1994)
- [23] G. Nuhn, W. Scheid and J.Y. Park, Phys. Rev C 35 (1987) 2146.
- [24] A. Thiel, J. Phys. G 16 (1990) 867.
- [25] J.Y. Park, W. Scheid and W. Greiner, Phys. Rev C 20 (1979) 188.
- [26] B. Imanishi and W. von Oertzen, Phys. Rep. 155 (1987) 29.
- [27] P. Ring and P. Schuck, in *The Nuclear Many-Body Problem*, (Springer-Verlag, 1980) p. 76.
- [28] Y.A. Ellis-Akorali, Nuclear Data sheets 52 (1987) 799.
- [29] M.J. Martin, Nuclear Data sheets 63 (1991) 723.
- [30] F. Ajzenberg-Selove, Nucl. Phys. A 490 (1988) 1.
- [31] M. Mirea, Phys. Rev C 54 (1996) 302.
- [32] A. Diaz-Torres, N.V. Antonenko and W. Scheid, Nucl. Phys. A 652 (1999) 61.
- [33] A. Diaz-Torres, G.G. Adamian, N.V. Antonenko and W. Scheid, Phys. Lett. B 481 (2000) 228.
- [34] G.G. Adamian, N.V. Antonenko, Yu. M. Tchulvil'sky, Phys. Lett. B 451 (1999) 289.
- [35] H.J. Krappe, J.R. Nix and A.J. Sierk, Phys. Rev. C 20 (1979) 992.
- [36] D.H.E. Gross and H. Kalinowski, Phys. Rep. 45 (1978) 175.
- [37] D. Glas and U. Mosel, Nucl. Phys. A 264 (1976) 268.

- [38] P. Fröbrich and R. Lipperheide, in *Theory of Nuclear Reactions*, (Claredon Press, Oxford 1996).
- [39] G.G. Adamian, N.V. Antonenko and R.V. Jolos, Nucl. Phys. A 584 (1995) 205.
- [40] H.H. Deubler and K. Dietrich, Nucl. Phys. A 277 (1977) 493.
- [41] H. Hofmann, Phys. Rep. 284 (1997) 139.
- [42] A. Diaz-Torres, G.G. Adamian, N.V. Antonenko and W. Scheid, Nucl. Phys. A 679 (2001) 410.
- [43] D. Glas and U. Mosel, Nucl. Phys. A 237 (1975) 429.
- [44] C. Ngô, Annu. Rev. Nucl. Part. Sci. 16 (1986) 139.
- [45] K. Arai, Y. Ogawa, Y. Suzuki and K. Varga, Phys. Rev. C 54 (1996) 132.
- [46] J. Galin et al., Phys. Rev. C 9 (1974) 1018.
- [47] A.H. Wapstra and G. Audi, Nucl. Phys. A 432 (1985) 1.

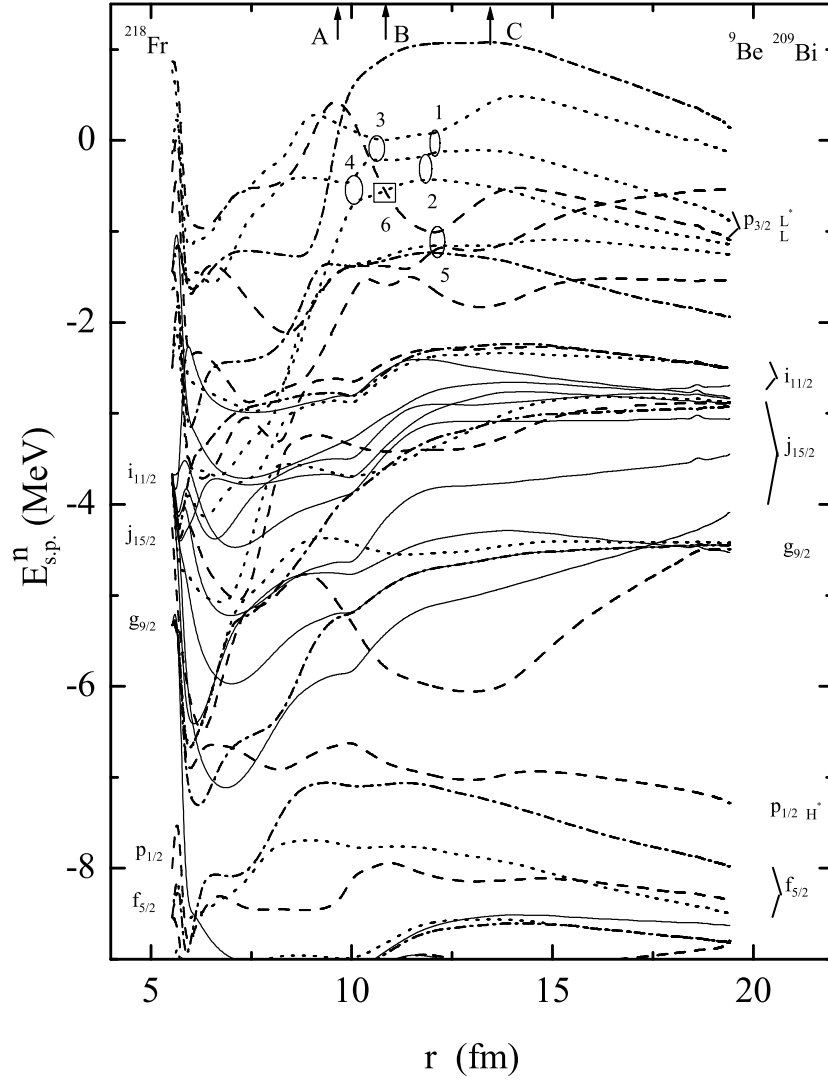


FIG. 1. Neutron levels for ${}^9\text{Be} + {}^{209}\text{Bi} \rightarrow {}^{218}\text{Fr}$ as a function of the separation r between the nuclei. Levels are characterised by the total angular momentum projection j_z on the internuclear axis: $j_z = 1/2$ (dashed curves), $j_z = 3/2$ (dotted curves), $j_z = 5/2$ (dashed-dotted curves) and other values (solid curves). See text for further details.

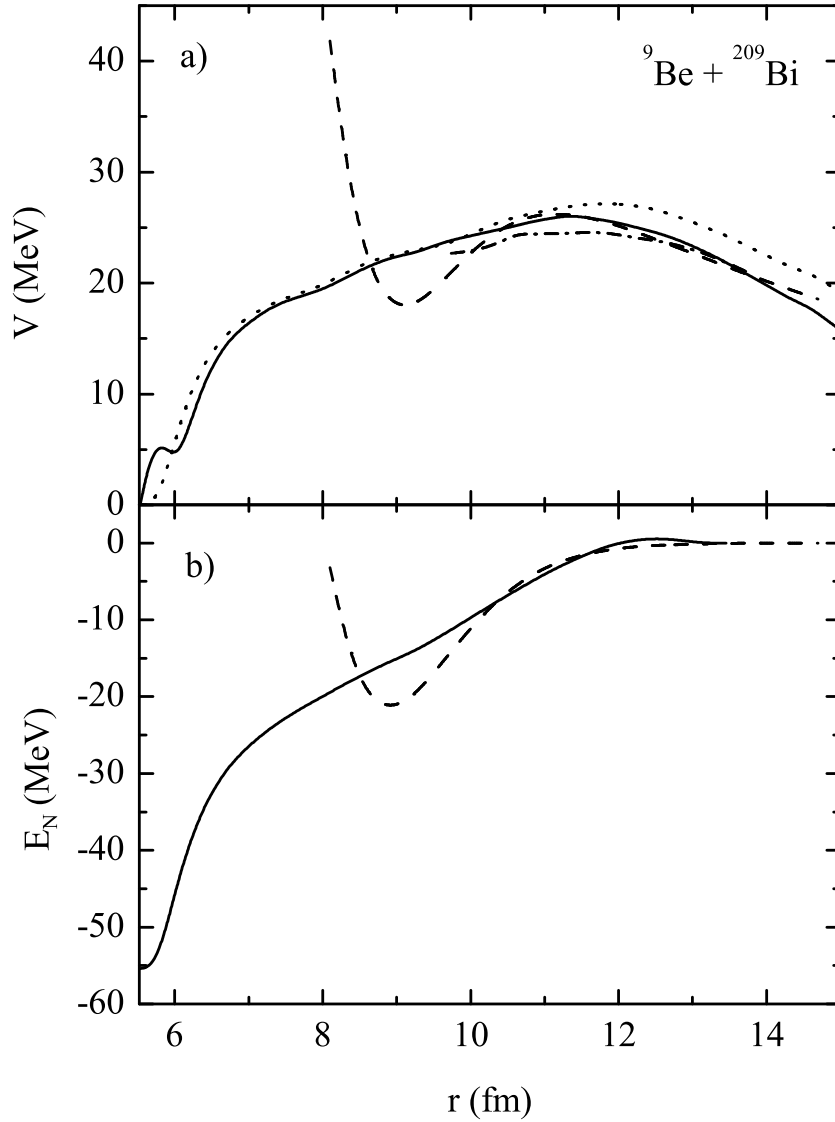


FIG. 2. a) The angular momentum independent part of the total nucleus-nucleus potential as a function of the separation r between the nuclei. The adiabatic TCSM-potential with spherical nuclei and the sudden double-folding potential are shown by solid and dashed curves, respectively. The smooth macroscopic part of the adiabatic TCSM-potential is presented by a dotted curve. The adiabatic TCSM-potential for the prolate nuclei in the pole-to-pole configuration is shown by a dashed-dotted curve. b) The nuclear surface energy E_N with spherical nuclei is shown by a solid curve. The nuclear double-folding potential is presented by a dashed curve. See text for further details.

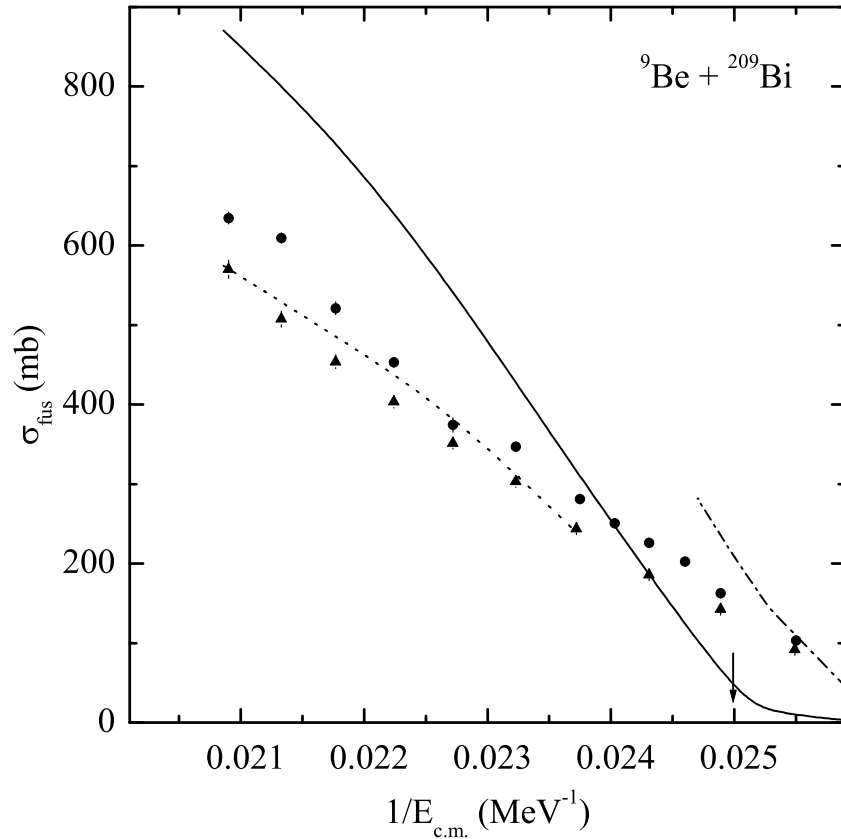


FIG. 3. Complete fusion cross sections σ_{fus} as a function of the inverse of the bombarding energy $1/E_{c.m.}$ in the center of mass system. Predictions (without breakup) of the Glas-Mosel model for the adiabatic TCSM-potential with spherical nuclei (see Fig. 2a) are shown by a solid curve and values taken into account the breakup of ${}^9\text{Be}$, by a dotted curve. Experimental data for the studied reaction (full dots) are from [10] and for ${}^9\text{Be} + {}^{208}\text{Pb}$ (full triangles) from [12]. Complete fusion cross sections σ_{fus} calculated with the Glas-Mosel model (without breakup) for the adiabatic TCSM-potential with prolate nuclei (see Fig. 2a) are presented by a dashed-dotted curve. See text for further details.

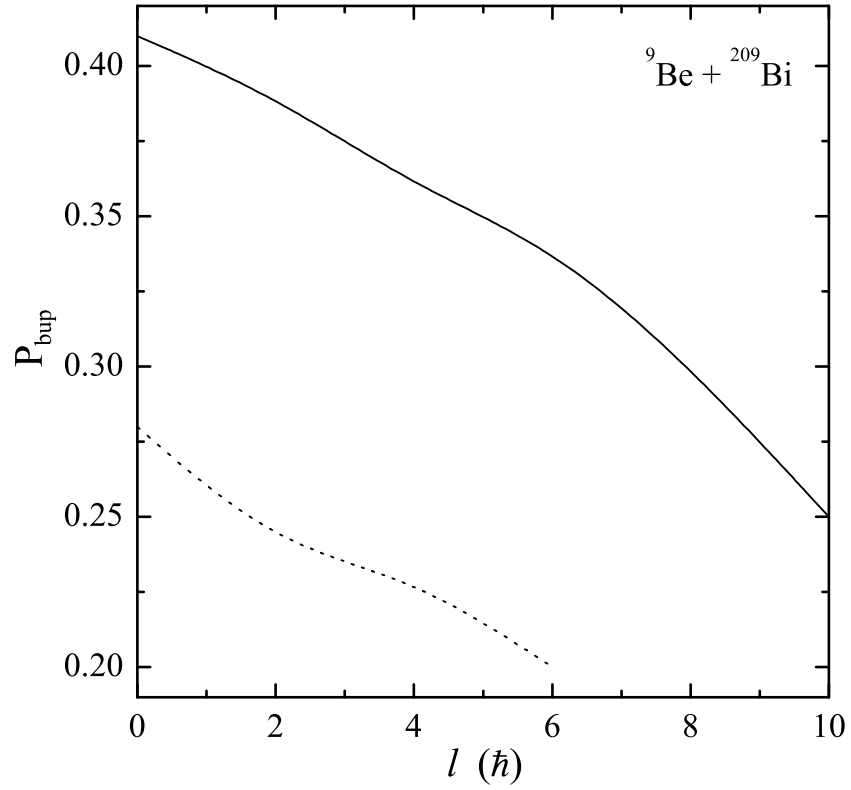


FIG. 4. Breakup probabilities P_{bup} as a function of the orbital angular momentum $l\hbar$ ($0 \leq l \leq l_{cr}$) for captured trajectories obtained for the adiabatic TCSM-potential with spherical nuclei (see Fig. 2a). Values for $E_{c.m.} = 42$ MeV and $E_{c.m.} = 46$ MeV are shown by dashed and solid curves, respectively. See text for further details.

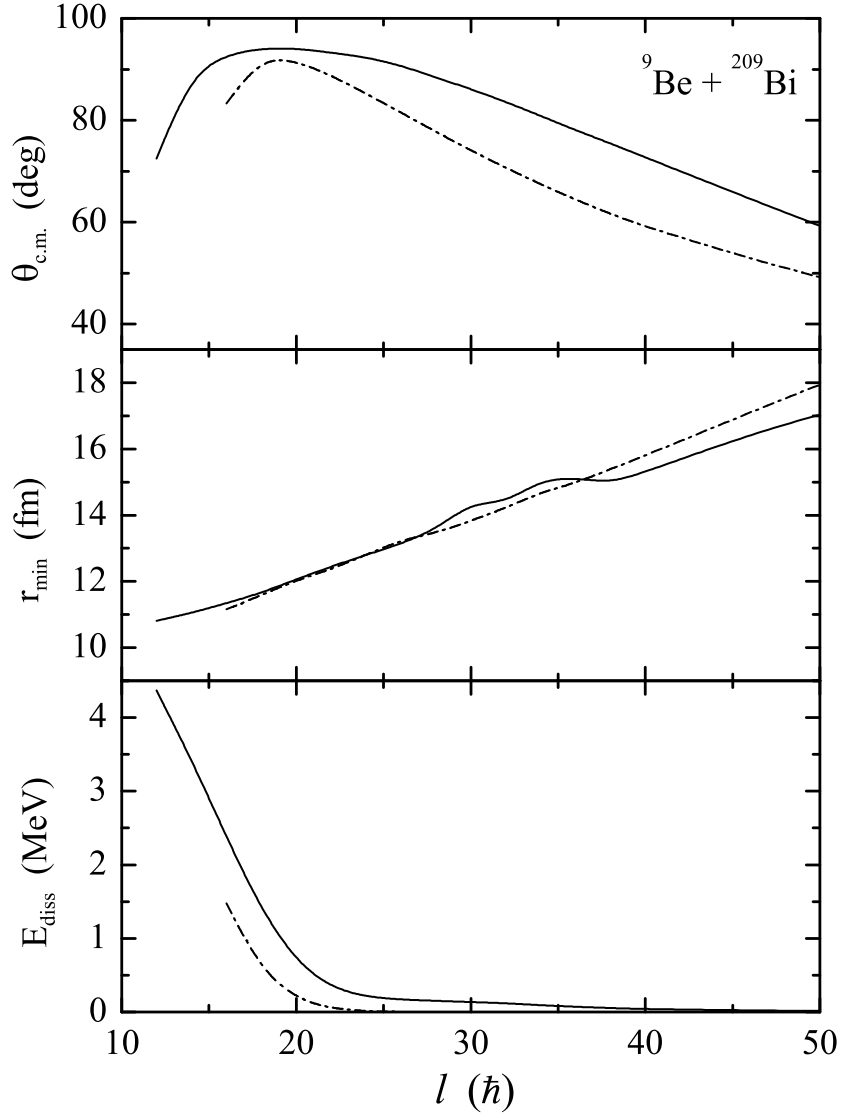


FIG. 5. Scattering function $\theta_{c.m.}(l)$ (upper part), distance of closest approach r_{\min} of the nuclei (middle part) and dissipated energy E_{diss} (lower part) as a function of the orbital angular momentum $l\hbar$ ($l > l_{cr}$) for non-captured trajectories at $E_{c.m.} = 46$ MeV. Values obtained for the adiabatic TCSM-potential with spherical nuclei (see Fig. 2a) and for the double-folding potential are shown by solid and dot-dashed curves, respectively. See text for further details.

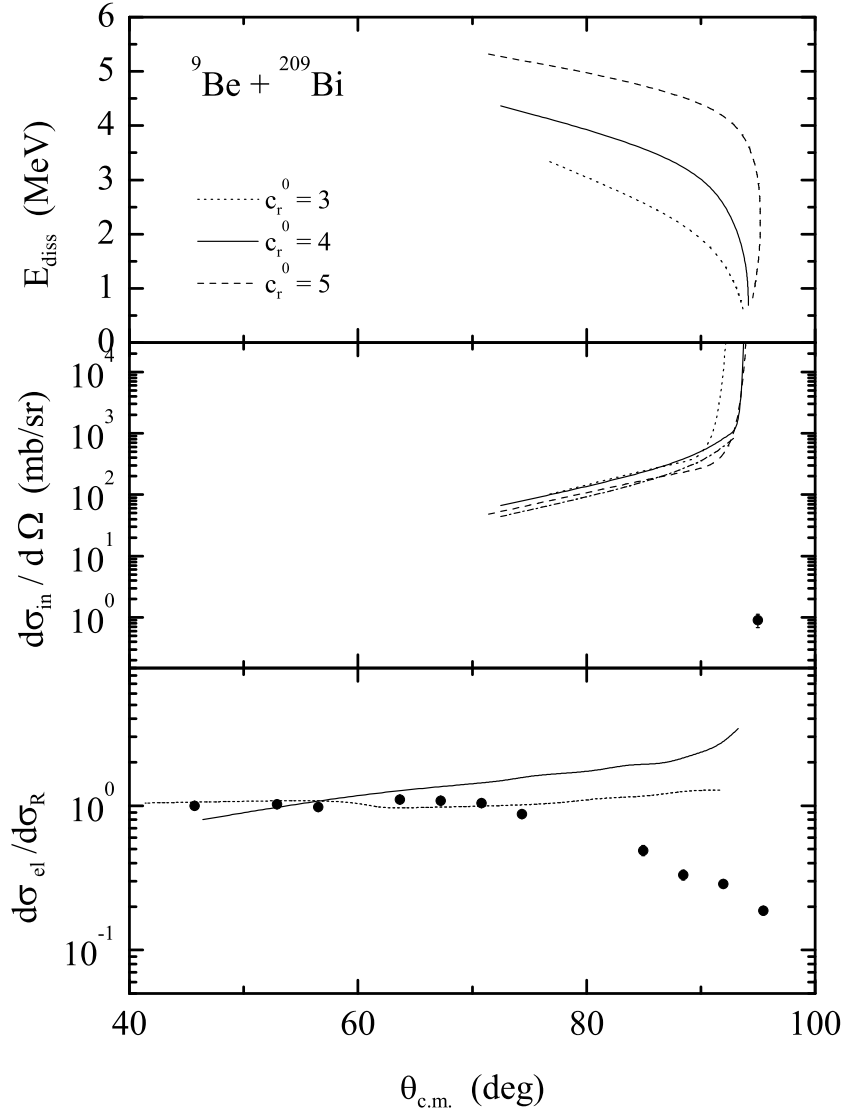


FIG. 6. At $E_{c.m.} = 46$ MeV, dissipated energies E_{diss} (upper part) and inelastic classical cross sections $d\sigma_{in}/d\Omega$ (middle part) as a function of the scattering angle $\theta_{c.m.}$ for inelastic non-captured trajectories obtained with the adiabatic TCSM-potential for spherical nuclei (see Fig. 2a) by using different values of the radial friction coefficient c_r^0 in units of 10^{-23} MeV $^{-1}$ s. For a radial friction coefficient $c_r^0 = 4 \times 10^{-23}$ MeV $^{-1}$, the inelastic angular distribution taking into account the breakup of ${}^9\text{Be}$ is shown by a dashed-dotted curve. The experimental point (full dot) is from [15]. Elastic angular distributions $d\sigma_{el}/d\sigma_R$ (lower part), normalised to the Rutherford cross section σ_R , obtained for the adiabatic TCSM-potential with spherical nuclei and for the double-folding potential are shown by solid and short-dashed curves, respectively. Experimental data (full dots) are from [15]. See text for further details.